

# Gas Pickering Emulsion Templated Hollow Carbon for High Rate Performance Lithium Sulfur Batteries

Matthew Li, Yining Zhang, Xiaolei Wang, Wook Ahn, Gaopeng Jiang, Kun Feng, Gregory Lui, and Zhongwei Chen\*

A CO<sub>2</sub> in water nanoparticle stabilized Pickering emulsion is used to template micrometer sized hollow porous nitrogen doped carbon particles for high rate performance lithium sulfur battery. For the first time, nanoparticles serve the dual role of an emulsion stabilizer and a pore template for the shell, directly utilizing in situ generated CO<sub>2</sub> bubbles as template for the core. The minimalistic nature of this method does not require expensive surfactants or additional core templates. Upon polymerization of melamine formaldehyde onto CO<sub>2</sub>, a robust polymer/silica composite shell is formed and transformed into a porous shell upon washing. The micrometer-sized hollow morphology in combination with its nitrogen rich porous shell demonstrates impressive rate capabilities of 670 and 500 mAh g<sup>-1</sup> even at a high rate of 7C and 9C, respectively. This material also possesses excellent cycle durability, exhibiting a low capacity decay of 0.088%/cycle over 300 cycles. Measurement of the shuttle current and impedance provides interesting insight into the polysulfide mass transfer mechanism of hollow structured sulfur hosts.

sulfur into the electrolyte, followed by its subsequent diffusion to the anode or more commonly known as the polysulfide (PS) shuttle effect. This causes unwanted side reactions ultimately resulting in poor cycle durability, low energy density, and low coulombic efficiency.<sup>[6b,7]</sup> A common strategy to mitigate the PS shuttle effect is to confine the PS within the cathode with host materials such as graphene foams,<sup>[8]</sup> various types of porous carbon,<sup>[6b,9]</sup> in addition to doped-carbon materials exhibiting PS adsorptive capabilities.<sup>[10]</sup> While LIS's stability and energy density is crucial, a high rate performance should be considered to be equally important and put under more scrutiny in the scientific community. In the case of electric vehicles (EV), the rate capability of the battery can influence the recharge time, acceleration, and regenerative braking efficiency. All

## 1. Introduction

Hollow structured nanomaterials have proven to be valuable throughout many different fields. The advantages of a hollow morphology stem from its unique implications in mass transfer characteristics such as physical separation of the core from the bulk phase.<sup>[1]</sup> Recognizing these benefits, researchers have explored innovative application in fields such as drug deliver,<sup>[2]</sup> waste water treatment,<sup>[3]</sup> among many others. One particularly interesting application of hollow morphologies is in energy storage,<sup>[4]</sup> specifically, the field of electrochemical batteries. Among many competing battery concepts,<sup>[5]</sup> lithium sulfur battery (LIS) has become one of the most extensively studied technologies, with promises of a five times increase in theoretical energy density (2500 Wh kg<sup>-1</sup>) compared to current lithium ion batteries.<sup>[6]</sup> Unfortunately, the full potentials of LIS are yet to be realized mainly due to the dissolution of

of these parameters directly affect the final user experience of the vehicle and can cause serious damage to the reputation of EVs if poorly implemented. Often researchers have achieved LIS with impressive cycle durability, coulombic efficiency, and capacity, but do not fare well when subjected to higher rate performance tests. Indeed, a complex pore network will limit PS diffusion and provide enhanced durability, but the very same tortuous diffusion pathway out of the cathode will inevitably increase lithium ion diffusion resistance. When combined with the known electrolyte viscosity/resistance increase upon PS dissolution,<sup>[11]</sup> it is understandable as to why the rate performance is poor. Recent research into the rate performance of LIS revolves around providing efficient lithium ion and electron mass transfer pathways<sup>[12]</sup> or additional battery components such as an interlayer to provide additional surface area for faster PS reduction kinetics.<sup>[13]</sup> Interestingly, hollow structures, which have been previously used to successfully address the stability problems of LIS, commonly demonstrate excellent rate performances.<sup>[9,14]</sup> The distinct difference between hollow porous structures and regular porous carbon lies in the separation of the core electrolyte from the bulk electrolyte phases. The shell can act as a physical barrier to encapsulate PS, limiting dissolution of active sulfur material into the bulk electrolyte. More importantly, the hollow structures can serve as a electrolyte reservoir<sup>[15]</sup> to redirect PS diffusion inwards and reduce the PS concentration in the bulk electrolyte. This mitigates the effects of the PS dissolution induced viscosity increase. Accordingly,

M. Li, Dr. Y. Zhang, Dr. X. Wang, Dr. W. Ahn, G. Jiang, K. Feng, G. Lui, Prof. Z. W. Chen  
Department of Chemical Engineering  
Waterloo Institute for Nanotechnology  
University of Waterloo  
200 University Ave West  
Waterloo, Ontario N2L 3G1, Canada  
E-mail: zhwchen@uwaterloo.ca



DOI: 10.1002/adfm.201603241

early work in hollow structures for LIS has demonstrated some of the highest rate performance of its time.<sup>[9,16]</sup>

Although hollow structures have been discovered for many years, it has always remained a type of novelty item in material science. Practical applications of hollow structures are limited due to relatively complex synthesis procedures. Most hollow carbon structures require the use of either chemical surfactants<sup>[14b,17]</sup> with two separate liquid phases<sup>[18]</sup> or hard templates,<sup>[9,14a]</sup> entailing complex and expensive synthesis processes. One solution can be the use of self-removing templates such as gas bubbles, which requires no additional core template removal step. However, regardless of the method chosen to template the core, to obtain a hollow structure with also a mesoporous shell requires the careful tuning of another set of template in addition to the core template. We look to solve this problem by taking advantage of the nanoparticle positioning in a Pickering emulsion (PE). First discovered by S. Pickering in 1907,<sup>[19]</sup> PE is a unique type of emulsion system that is stabilized not by surfactants, but by particles.<sup>[20]</sup> The stabilized emulsion droplet is therefore composed of a multilayer nanoparticle shell, of which we conveniently used as pore templates for the shell.

Herein, to the best of our knowledge we report for the first time the design and development of a CO<sub>2</sub> PE templated micrometer sized hollow nitrogen doped porous carbon for high rate performance lithium sulfur battery. This novel synthesis technique demonstrates low material cost and facile synthesis compared to other methodologies. The hollow morphology is

achieved by first obtaining a CO<sub>2</sub> in water PE and then utilizing the CO<sub>2</sub> bubbles as a template for the hollow core through polymerization of melamine. Conveniently, no premade CO<sub>2</sub> emulsion solution is required, and no additional hard/soft templates or liquid phases are required to form the hollow core. By polymerizing the carbon precursor around the nanoparticles stabilized emulsion, a porous shell can be obtained. This procedure effectively unites the normally separate: core templating and shell templating process, into one facile step. Through the combination of the hollow structure, and nitrogen doping, superior rate performance is obtained.

## 2. Results and Discussion

To synthesize the hollow carbon, Na<sub>2</sub>CO<sub>3</sub> is added to increase the pH to react melamine with formaldehyde. Subsequently, nanoparticles (silica) are dispersed into the prepolymer solution prior to gas bubble generation, priming the system for PE formation. 2 M HCl is then added to the solution to lower the pH, for first the generation of CO<sub>2</sub>, and then the initiation of melamine formaldehyde (MF) polymerization. The proposed synthesis flow chart of the Pickering emulsion stabilized hollow porous carbon is presented in **Figure 1**. Once the pH is adjusted from 9.5 to 7, Na<sub>2</sub>CO<sub>3</sub> reacts with HCl and generates CO<sub>2</sub> gas. The CO<sub>2</sub> gas bubbles are then encapsulated by silica particles, forming a PE. When the pH is lowered to 5.5, the polymerization and crosslinking of MF begins to form a robust silica/MF

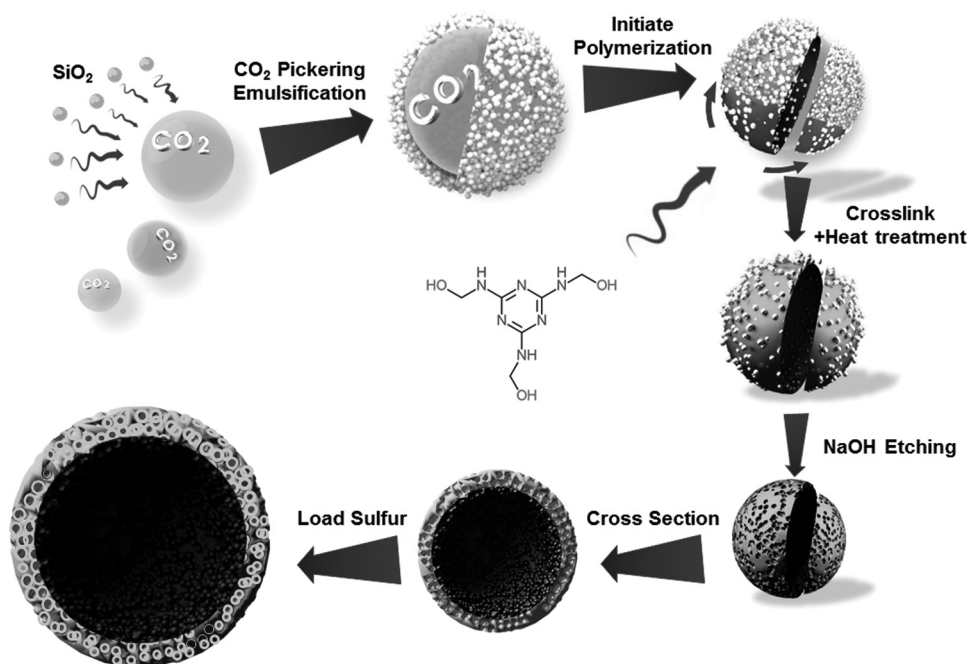


**Figure 1.** Illustration of proposed synthesis mechanism. Briefly, HCl is added into a basic (Na<sub>2</sub>CO<sub>3</sub>) melamine formaldehyde prepolymer solution with silica dispersed homogenously. The first purpose of the HCl is to initiate the polymerization and crosslinking of melamine formaldehyde monomers. The second purpose is to generate CO<sub>2</sub> gas bubbles in situ inside the solution. At higher agitation rates and correct pH, the silica nanoparticle diffuses to the surface of these CO<sub>2</sub> bubble to form a silica stabilized CO<sub>2</sub> Pickering emulsion in water. Subsequently, the melamine formaldehyde monomers begin to phase separate out of water and polymerize onto the silica covered CO<sub>2</sub> bubbles. After the monomer is crosslinked, the hollow morphology is casted and solidified. After carbonization and silica removal, a nitrogen doped hollow carbon with a porous shell is obtained. Sulfur is the loaded into the shell of the porous carbon.

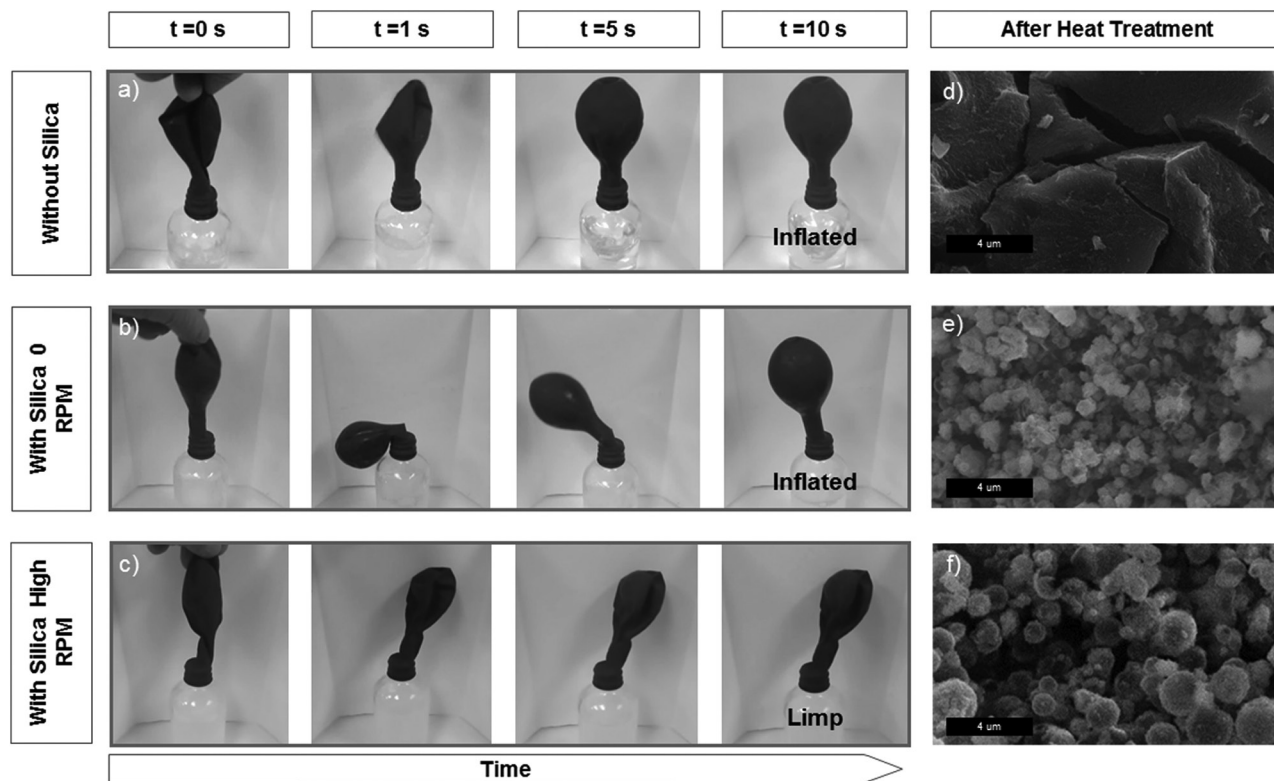


**Figure 2.** Image of balloon inflated by generated  $\text{CO}_2$  at different time steps after HCl addition a) without silica at high agitation rate; b) with silica at 0 RPM; c) with silica at high RPM; d) SEM image of morphology without silica template; e) with silica at low RPM; and f) with silica at high RPM.

composite shell around the  $\text{CO}_2$  bubbles. Upon curing, the hollow morphology is casted. To further explore and elucidate the synthesis mechanism, **Figure 2a–c** presents an experiment where 2 M HCl is added into a solution of  $\text{Na}_2\text{CO}_3$  (without MF at pH 9.5) until the pH is lowered to 5.5 with a balloon covering the solution. Immediately, the reaction between HCl and  $\text{Na}_2\text{CO}_3$  generates  $\text{CO}_2$  and inflates the balloon. The degree of inflation provides an indication as to how much  $\text{CO}_2$  is released from the solution and how much is emulsified. Aligning with our expectations, a significant difference is found if certain experimental conditions are adjusted. Specifically, three different scenarios are investigated: without silica, i.e., no emulsifying agent (**Figure 2a**), with silica but no agitation (**Figure 2b**) and with silica in addition to rigorous agitation (**Figure 2c**). In the case without silica (**Figure 2a**), the produced  $\text{CO}_2$  gas is captured by the blue balloon and inflates it. This is understandable as there are no emulsifying agents (silica) present to stabilize the  $\text{CO}_2$  bubbles. One might suggest MF to be an important or even the dominant  $\text{CO}_2$  emulsifying agent, implying the inflation of the balloon is caused by the absence of MF. If MF does indeed serve a more important role over silica in  $\text{CO}_2$  emulsification then the absence of silica should have little effect on the morphology. This is revealed not to be the case. When the synthesis procedure is carried out without silica, the resulting scanning electron microscopy (SEM) image of the morphology (**Figure 2d**) reveals no hollow morphology. Hence, there exists a requirement of silica particles in the formation of hollow structure.

In **Figure 2b**, prior to HCl addition, silica is added into the  $\text{Na}_2\text{CO}_3$  solution. After dispersing the silica, 2 M HCl is added without agitation. The generated  $\text{CO}_2$  once again inflates the blue balloon, indicating no  $\text{CO}_2$  emulsification. In **Figure 2c**, the same experiment is performed, but this time with vigorous agitation while HCl is being added. The result is a limp blue balloon. The decreased inflation of the balloon indicates that the volume of  $\text{CO}_2$  is compressed. Gas bubbles are at higher pressures than its bulk phase to balance the surface tension inherent to its spherical geometry. The contrast between **Figure 2b,c** is interesting and indicates that if the solution is not agitated, even the presence of nanoparticles (silica) cannot form  $\text{CO}_2$  emulsions. This illustrates an important relationship between the encapsulation of  $\text{CO}_2$  bubbles and the agitation rate, characteristic to bringing a system to a thermodynamically unstable state, i.e., emulsion.<sup>[21]</sup> More importantly, this same relationship is found in the morphological results when applied to synthesis conditions. When the synthesis is carried out at low rotations per minutes (RPM) such as 300 RPM, almost no hollow spheres are found (**Figure 2e**), whereas at 1200 RPM, almost all MF/silica composites are in their hollow form (**Figure 2f**). Additionally, NaOH is used to substitute  $\text{Na}_2\text{CO}_3$  in synthesizing the MF prepolymer solution as another control experiment. This eliminates any possibility of  $\text{CO}_2$  formation and should yield no hollow structure. Aligning with our theory, the final result reveals no spherical/hollow morphology (**Figure S1**, Supporting Information).

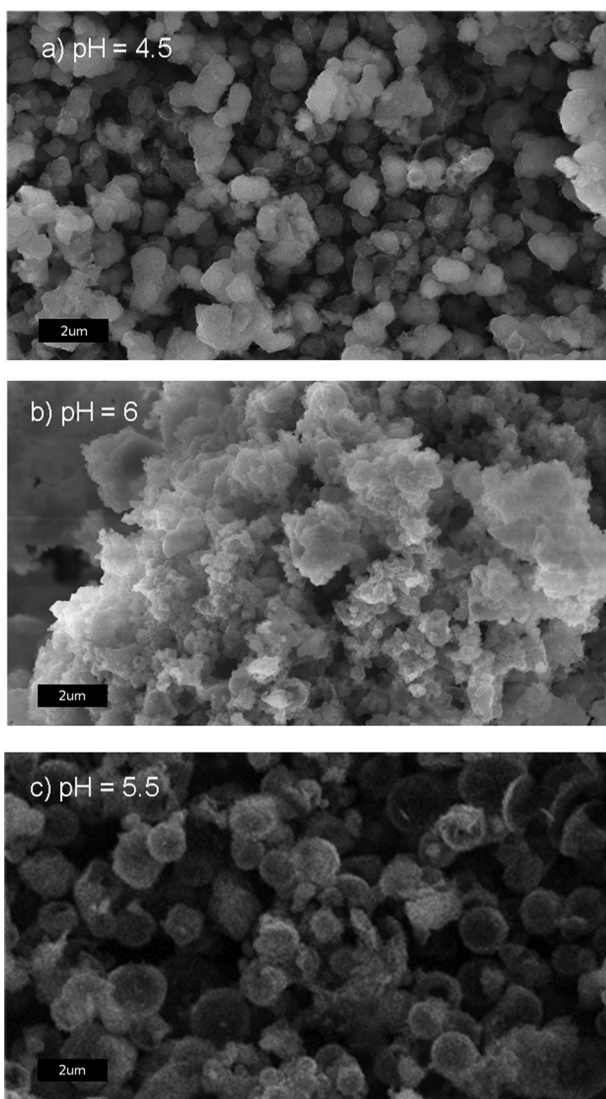


**Figure 3.** SEM image of sample with synthesis carried out at a) pH 4.5, b) pH 6.5, and c) pH 5.5.

The particle's morphology is also strongly dependent on the pH of the solution. When the pH value is held at 4.5 or 6.0 instead of 5.5, no hollow morphology is present, as seen in **Figure 3a,b**. CO<sub>2</sub> is widely known to be in equilibrium with carbonic acid when dissolved in water, and the equilibrium shifts depending on the pH. If the pH is too low, the equilibrium will shift toward CO<sub>2</sub> and increase the rate of CO<sub>2</sub> generation. At a sufficiently low pH, the high rate of CO<sub>2</sub> generation can overcome the rate of emulsification, and result in the release of CO<sub>2</sub> into the atmosphere. Without CO<sub>2</sub> acting as the hollow core template, the resulting particles (**Figure 3a**) reveal no spherical morphology even at high RPM. On the other hand, if the pH is too high, the equilibrium will shift toward the carbonic acid. In this case, there are not enough CO<sub>2</sub> bubbles which allows the polymerization of MF to exceed that of CO<sub>2</sub> emulsification, resulting in formation of randomly seeded porous carbon particle without a hollow core. Again, the resulting SEM imaging of the morphology confirms no spherical morphology even at

high RPM (**Figure 3b**). However, when the pH is kept at 5.5, in between 4.5 and 6, the resulting morphology reveals the desired spherical morphology (**Figure 3c**). Therefore, the pH can be used to effectively tune the rate of CO<sub>2</sub> release into the solution. From our experiments, perfect tuning can be defined as the pH at which the CO<sub>2</sub> release rate matches the rate of CO<sub>2</sub> emulsification.

These experiments show that CO<sub>2</sub>, silica, correct pH tuning, and a sufficiently high agitation rate are all required to form a hollow morphology. Furthermore, literatures have demonstrated that silica can form PEs.<sup>[20a,f]</sup> It should also be noted that a gas/water emulsion will quickly coalesce or phase separate due to differences in density if left stagnant and will cause the CO<sub>2</sub> to lose its function as a hollow-structure template. Because of the relative instability of gas emulsion systems,<sup>[22]</sup> carbon precursors that do not adhere strongly to the nanoparticle stabilized gas emulsion droplets, but are merely adsorbed onto the surface, cannot form hollow carbon particles. This problem is circumvented in this work due to the polymerization of MF shortly after CO<sub>2</sub> emulsion formation. Not only can the prepolymer solution act as an emulsion costabilizer,<sup>[23]</sup> but once the pH is lowered past 7, MF begins to polymerize appreciably, and crosslink around each individual silica particle on the emulsion droplet. This forms a denser, mechanically robust MF/silica composite which consolidates the positioning and preserves the hollow morphology of the PE. Ultimately, this new synthesis methodology creates a MF/silica composite as the shell of a hollow particle. This brings forward another important role of silica. In addition to being an emulsion stabilizer, silica also conveniently acts as a hard template to form mesopores throughout the shell.

The benefits of this method lie in the use of gas bubbles as template for the hollow core. No prior preparation of a micro-bubbles solution is required such as<sup>[23]</sup> and no additional surfactants are required to facilitate the formation of this hollow morphology. This procedure is only a slight modification (change of reaction RPM and pH) of traditional hard templating porous carbon synthesis techniques, but effectively transforms a simple porous carbon particle into a porous carbon shell-hollow sphere. In this work, silica nanoparticles is selected as the CO<sub>2</sub> emulsion stabilizer due to its relatively low cost and commercial availability, but other nanoparticles can also be utilized to form PEs, depending on the application.<sup>[24]</sup> Conceptually novel, the dual role of the nanoparticle in this system serves both as an emulsifying agent and a pore template. We believe this method can be carried over to many different combination of carbon source/pore template.

After carbonization, the resulting hollow morphology is studied under a transmission electron microscope (TEM), **Figure 4a** depicts a single hollow carbon sphere prior to silica removal. Higher magnification TEM (**Figure 4b**) at the edge of the particle reveals multiple layers of  $\approx 23$  nm particles (silica) on the surface. This provides evidence that silica particles are on the surface of the gas bubble, confirming silica's role as an emulsifying agent for CO<sub>2</sub>. After removal of silica, a  $\approx 60$  nm thick porous shell remains. The pores on the shell are confirmed by **Figure 4d**, revealing pores sizes of  $\approx 23$  nm which aligns with the size of the silica nanoparticle used. This confirms the high dispersion of silica on the surface of the CO<sub>2</sub> and

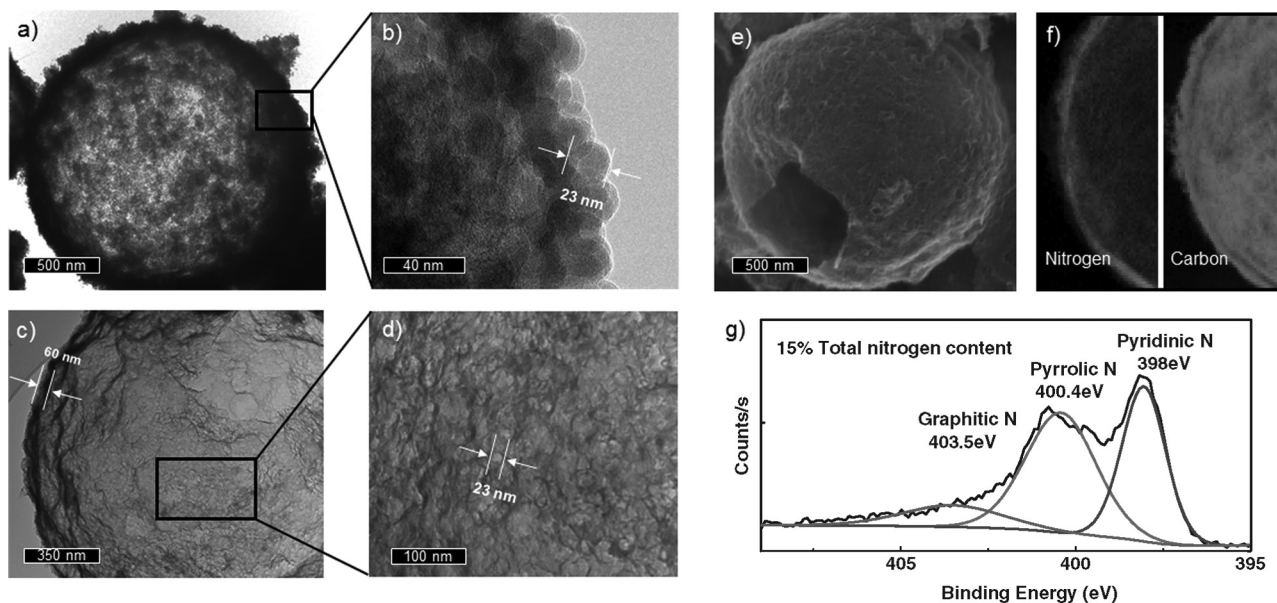


**Figure 4.** a) TEM image of single PEHPC with silica; b) TEM image of shell of PEHPC indicating  $\approx 20$  nm silica particle; c) TEM image of a single PEHPC revealing shell of  $\approx 60$  nm; d) TEM of shell of PEHPC revealing pores of  $\approx 20$  nm; e) SEM image of a single broken PEHPC revealing hollow core; f) EELS mapping of nitrogen and carbon; and g) XPS binding energy spectrum of PEHPC.

throughout the MF composite and more importantly, confirms its function as a mesopores template. The hollow morphology is again shown through SEM imaging, Figure 4e depicts a single broken particle after silica removal revealing a hollow core. The final material after silica etching will be referred to as Pickering emulsion hollow porous carbon (PEHPC).

Due to the use of melamine as carbon precursor, PEHPC possesses nitrogen doping. Electron energy loss spectroscopy (EELS) is employed to investigate distribution of nitrogen doping (Figure 4f). It is found that nitrogen is dispersed homogeneously throughout the structure with very strong signals throughout. Finally, nitrogen doping in PEHPC is examined by X-ray photoelectron spectroscopy (XPS) analysis (Figure 4g). The graphitic, pyridinic, and pyrrolic form of nitrogen represents 12.5%, 39%, and 48.5% of the total nitrogen content respectively. It is important to note that the graphitic nitrogen has been shown through multiple density function theory calculations<sup>[10,25]</sup> to possess the least amount of interaction with PS, while the pyridinic and pyrrolic have a significantly higher affinity to adsorb PS. Therefore, to make the best use of nitrogen doping, the graphitic form should be minimized. Our material has the advantage of possessing a relatively low graphitic nitrogen content of 12.5%, while maintaining a high percentage of both pyrrolic and pyridinic nitrogen. Moreover, the overall total nitrogen content of PEHPC (15 at%) is among some of the highest nitrogen doping content for hollow porous carbon structure.<sup>[17b,26]</sup>

As expected, PEHPC demonstrates impressive capabilities as a sulfur host for LIS. Figure 5a indicates that at high discharge rates of 7C and even up to 9C, PEHPC loaded with 70% sulfur delivers a capacity of  $\approx 670$  mAh g<sup>-1</sup><sub>sulfur</sub> and  $\approx 500$  mAh g<sup>-1</sup><sub>sulfur</sub>, respectively. In contrast, the Ketjen black 600 JD (KB) electrode is found to deliver a significantly lower, 335 mAh g<sup>-1</sup> at only a rate of 5C. At higher rates such as 9C, the KB electrode is

only able to deliver 113 mAh g<sup>-1</sup>. The impressive performance of PEHPC can be due to a combination of three properties of PEHPC. First, nitrogen doping had been previously speculated to possess catalytic properties toward the reduction of PS.<sup>[27]</sup> This can serve to lower the impedance in the cell and allow for more reduction of polysulfide species. Second, owing to the micrometer sized nature of PEHPC, the interparticle spacing can allow for very efficient lithium ion mass transfer compared to smaller sized hollow carbon.<sup>[28]</sup> Third, due to the hollow core, PS diffusion is directed inward due to a concentration gradient. An inward PS flux obtains a portion of the PS and decreases the amount of PS diffusion into the bulk electrolyte. One commonly overlooked problem of LIS is the corresponding increase in viscosity due to increases in PS concentration. The increase in viscosity is highest during the end of the 1st plateau, when all solid S<sub>8(s)</sub> has been reduced to its soluble S<sub>8</sub><sup>2-</sup>, S<sub>6</sub><sup>2-</sup>, and S<sub>4</sub><sup>2-</sup> form.<sup>[29]</sup> At this time, the lithium ion transfer will be significantly retarded. This will cause the cell to prematurely reach the cut-off voltage, resulting in very poor rate performances. At high discharge rates, the ability of the cell to discharge is drastically decreased by the lack of Li<sup>+</sup> ion mass transfer through the viscous electrolyte. We believe in the case of PEHPC, some of the PS are redirected inward, partially relieving the bulk electrolyte of PS and lowers the overall viscosity of the bulk electrolyte. The ability of PEHPC to discharge at 9C can have significant implication in the rate performance aspects of electric vehicles.

Additionally, PEHPC also exhibits exceptional cycle durability. Long galvanostatic cycling at 0.5C (Figure 5b) reveals that PEHPC delivers 980 mAh g<sup>-1</sup><sub>sulfur</sub> and continues to retain a capacity of 720 mAh g<sup>-1</sup><sub>sulfur</sub> (73% retention) at the 300th cycle (0.088% capacity loss/cycle). This impressive cycle life is most likely due to the combined effect of the hollow structure in addition to the high nitrogen doping content (15 at%) of PEHPC, in

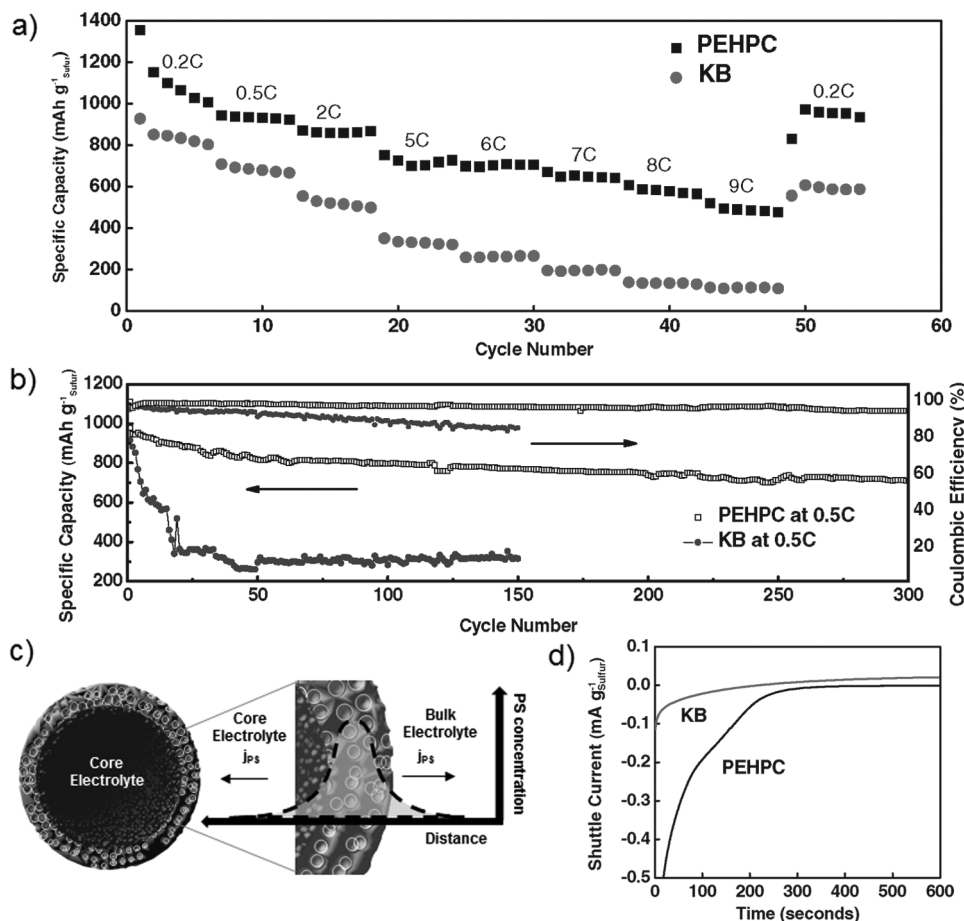


**Figure 5.** Rate performance of a) PEHPC and KB; b) cycling capacity and coulombic efficiency of PEHPC and KB at 0.5C; c) illustration of PS diffusion mechanism of hollow structures; and d) time profile of the shuttle current of KB and PEHPC.

alignment with previous studies.<sup>[26g]</sup> Additionally, most of the nitrogen groups in PEHPC are found to be in the pyridinic and pyrrolic form. It has been theorized that the graphitic nitrogen can provide a permanent dipole on the carbon structure due to differences in electronegativity between N and C. However it has been shown that such dipole interactions with PS species are minimal when compared to the Lewis base like characteristics of the lone pair in the pyridinic and pyrrolic nitrogen groups.<sup>[10b,30]</sup> Hence the large amount of pyrrolic and pyridinic nitrogen sites throughout PEHPC can be seen as a bin that retards any diffusion of PS away from each PEHPC particle by adsorbing and holding onto PS. The advantage of using PEHPC as a sulfur host is evident when comparing against KB. The cycling result indicates an initial cycle of  $\approx 900 \text{ mAh g}^{-1}_{\text{sulfur}}$  at 0.5C, lower than that of PEHPC and quickly decreases to  $320 \text{ mAh g}^{-1}$  (36% retention) at the 150th cycle, representing a severe capacity loss of 0.43%/cycle. Owing to the effects of  $\text{LiNO}_3$ , the coulombic efficiency of the KB electrode is still relatively high (>85%) over 150 cycles, indicating suppressed reduction of PS species on the lithium anode. However, the inability of the KB to locally retain PS can result in the redistribution of sulfur throughout the cathode. Once redistributed, the sulfur becomes electronically inaccessible and causes severe cycle degradation. Additionally, the coulombic efficiency of PEHPC (93%

at 300th cycle) is also significantly higher than that of KB (85% at 150th cycle). The higher coulombic efficiency further corroborates the fact that PEHPC is superior to KB in mitigating both the effects of the PS shuttle effect and in managing the redistribution of PS throughout the electrode.

The observed rate performance and cycle durability is most likely due to the hollow structure. The distinct difference between porous carbon and hollow porous carbon lies in the separation of the electrolyte phases. Electrolyte can be categorized into two types: the bulk electrolyte, the portion that is outside of the core and in between the PEHPC particles, while the core electrolyte is the portion that resides at the core of PEHPC as shown in Figure 5c. The core electrolyte is an especially interesting feature of PEHPC and provides unique mass transfer dynamics. As PS molecules are generated in the shell, a corresponding concentration gradient (shown in orange) would be present both inward and outward. The outward diffusion of PS will be obviously poor for PS retention but the inward diffusion will allow the void core to act as a PS concentration sink. The inward PS flux/diffusion works to deplete the PS in the porous shell, lowering its concentration. The shell with a now lowered outward concentration gradient, generates a lowered outward flux. Moreover, the PS in the core of any specific PEHPC particle can only be reduced/oxidized

exclusively by that same PEHPC particle. Through the unique mass transfer mechanics of hollow structures and PS adsorption of nitrogen doping, PEHPC is able to achieve high rate performance and stable cycle life. To further investigate this phenomenon, measurement of the shuttle current (SC) is performed according to the work done by Moy et al.<sup>[31]</sup> The SC is a quantification of the amount of PS diffusion from the cathode to the anode. In short, the shuttle current can be obtained by first charging the cells to 2.8 V, followed by holding the cell at a constant 2.3 V, and then measuring the current response versus time. Initially, the current will be negative (discharging) because of the reduction of PS species that can thermodynamically be reduced at 2.3 V. As time proceeds, the discharge current decreases due to depletion of all reducible species (at 2.3 V) in the electrolyte, and reaches zero. However, the current does not remain at zero because of the PS shuttle effect. Due to PS diffusion toward the anode, the lithium constantly consumes PS species, resulting in the well-known self-discharge phenomenon and lowers the voltage of the cell.<sup>[32]</sup> In order to maintain the cell voltage at 2.3 V, the current must now switch from negative (discharging) to positive (charging), oxidizing the lower order PS at the cathode to high order PS at a rate that matches the rate of PS diffusion away from the cathode/self-discharge. Therefore, the current time profile can be viewed as the real-time result of the ongoing competition for PS mass between cathode reduction and PS self-discharge. When all reducible species has been reduced and the system has reached steady state, the corresponding steady state current matches exactly that of the rate of PS diffusion, i.e., the shuttle current.<sup>[31]</sup> In the case of this work, the transient component of the SC time profile is more informative because it provides insight as to how exactly this steady state current is reached and sheds light on the PS mass transfer dynamics prior to consumption. Figure 5d reveals that at  $\approx 100$  s, the transient component of PEHPC possesses a distinct decrease in the rate of change (inflection point) of the current. The inflection point indicates that some factor in the cell is suddenly providing PS for the cathode to discharge, slowing the onset of a positive/charging steady state current. This is intriguing because in the case of a hollow morphology, the concentration profile in the core during SC measurement will also be time dependant. Initially, it will be lower than the shell (promoting an inward flux), but eventually, all PS in the shell will be depleted and the PS concentration in the core will be higher than the shell. We therefore attribute the inflection point to the reversal in PS flux resulting in PS diffusion from the core to the shell. The funneling of PS species from the core to the conductive shell allows for the cell to maintain a higher discharge current for an extended period of time. Once the core PS concentration is depleted, the current will then reach the steady state SC. One might argue that pores in KB can serve the same purpose, since the interparticle void space can function as PS mass sinks and should demonstrate the same SC time profile. This is experimentally shown to be not the case, because the KB SC time profile quickly reached steady state upon holding at 2.3 V. This indicates a possible dependence of the shuttle current profile on the local void space size as oppose to the total magnitude of the void volume. The contrasting transient SC profile between PEHPC and KB provides interesting evidence of the

beneficial effects of hollow morphologies while, at the same time, offers valuable insight into the mass transfer mechanism involved.

Finally, if the PEHPC can indeed redirect the PS diffusion inward then there should be some significant difference in the electrolyte resistance between PEHPC and KB electrodes. To confirm this theory, electrochemical impedance spectroscopy (EIS) measurements are performed at various depth of discharge (DOD). A “snapshot” of various circuit parameters ( $R_e$ ,  $R_{ct}$ , and  $R_{int}$  shown in Figure 6b–d, respectively) is revealed at different DOD. Figure 6a indicates the DOD locations of EIS captures with black and red squares for both PEHPC cell and KB cell (respectively) during 1st discharge at 0.1C. The circuit that is used for fitting is shown in the bottom portion of Figure 5b, identical to the circuit in work by Yuan et al.<sup>[29]</sup>  $R_e$  is normalized to the  $R_e$  of a fresh cell, this is done to deconvolute any differences in electrical connection between KB and PEHPC. If the viscosity of the electrolyte is to be controlled, there should be drastic difference between KB's and PEHPC's  $R_e$  value throughout discharge. As seen in Figure 6c,  $R_e$  initially increases for both KB and PEHPC due to the dissolution of PS, and as expected, decreases once the soluble PS converts to solid  $\text{Li}_2\text{S}$  products. Aligning with our expectations, KB experiences a much higher increase in electrolyte resistance throughout discharge ( $\approx 280\%$  increase) when comparing to PEHPC ( $\approx 72\%$  increase), indicating PEHPC is able to indeed limit PS dissolution into the bulk. The  $R_{ct}$  for PEHPC is higher than that of KB from 0% to 20% DOD. However, once 20% DOD is reached, KB's  $R_{ct}$  appears to increase while PEHPC decreases. This supports our speculation that the viscosity increases more for KB than for PEHPC. With a higher PS concentration the  $R_{ct}$  of KB increases. Whereas in the case of PEHPC, the effect of PS dissolution on  $R_{ct}$  is insignificant. Instead,  $R_{ct}$  is observed to decrease continuously throughout discharge for PEHPC. This is most likely because the insulating solid sulfur material is consumed throughout discharge, relieving the conductive network of some charge transfer resistance.

$R_{int}$  value for PEHPC also starts at a much higher value than that of KB and remains higher from 0% to 50% DOD. This is most likely due to the higher electrical conductivity of commercial KB compared to our in-house-made carbon material. Interestingly, upon reaching 30% DOD in the KB electrode (corresponding to the beginning of the 2nd plateau), a sharp increase in  $R_{int}$  is observed. This is to be expected as the precipitation of  $\text{Li}_2\text{S}$  occurs during the 2nd plateau. At  $\approx 50\%$  DOD, the interfacial resistance for KB increases past PEHPC. This is most likely due to the inability of KB to retain PS in a localized region, resulting in random precipitation and agglomeration of  $\text{Li}_2\text{S}$  throughout the electrode. These  $\text{Li}_2\text{S}$  agglomerates greatly increase the interfacial transfer of electrons, whereas PEHPC is able to retain PS in the core, limiting redistribution. Hence, no increase in interfacial resistance is observed. By lowering viscosity of the bulk electrolyte and the corresponding resistance in the cell, PEHPC is able to deliver  $\approx 500$  mAh  $\text{g}^{-1}_{\text{sulfur}}$  at 9C. Both the nitrogen doping and partial redirection of PS diffusion ensures a much larger population of sulfur participated in the reduction reaction even at a high 9C discharge rate.

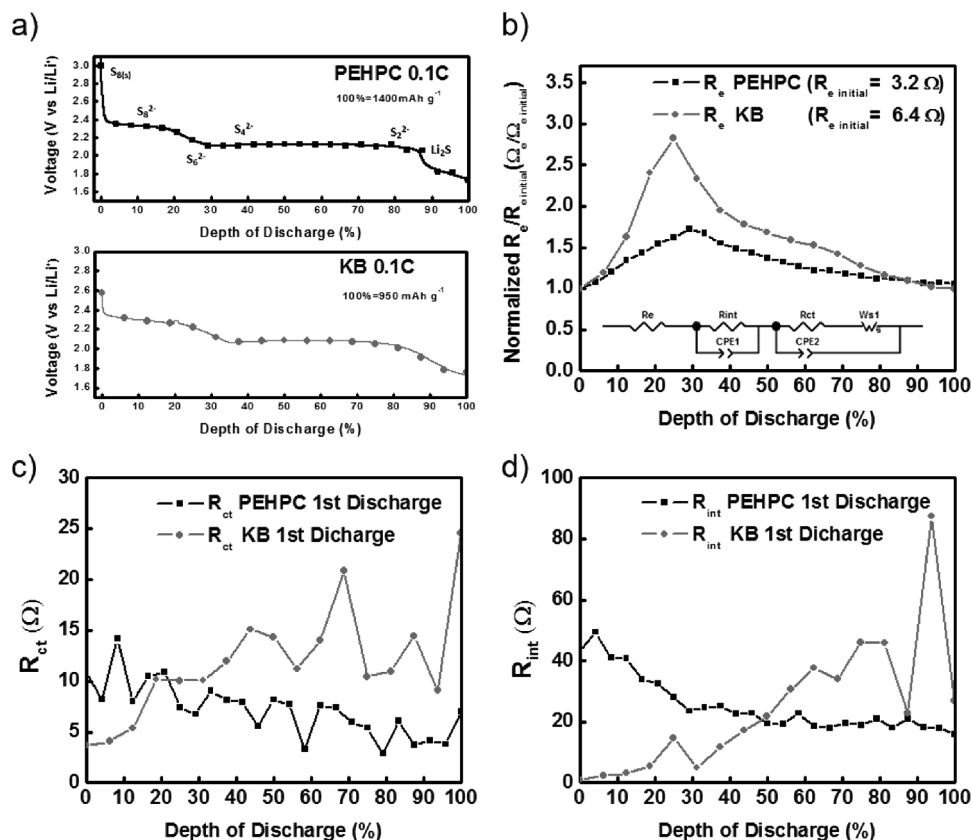


**Figure 6.** a) First discharge voltage profile at 0.1C with squares indicating DOD at which EIS measurements were performed; b)  $R_e$ , c)  $R_{ct}$ , and d)  $R_{int}$  at various DOD for PEHPC and KB.

### 3. Conclusion

A novel method was employed to synthesize a micrometer-sized hollow carbon with a nitrogen doped porous shell through the use of a Pickering emulsion. Melamine formaldehyde resin was used to polymerize and crosslink over the CO<sub>2</sub> emulsion, consolidating and casting the delicate hollow morphology. The mechanism was revealed to be strongly dependant on the degree of agitation and the pH of the solution. PEHPC was used as a sulfur host for lithium sulfur battery and demonstrated impressive rate performance up to 9C and excellent cycle stability. In order to understand the superior performance of PEHPC, the shuttle current and EIS measurements were conducted. PEHPC revealed an interesting transient shuttle current profile when compared to the KB cells, providing a window into understanding the rich mass transfer dynamics of hollow structures for sulfur battery application. Electrochemical impedance spectroscopy revealed a drastic difference between the electrolyte, charge transfer and interfacial resistance of PEHPC and KB providing further evidence on the effects of a hollow nitrogen doped structure. We attributed these results to the inward diffusion of PS, which alleviated the viscosity increase experienced by the bulk electrolyte.

### 4. Experimental Section

**Material Synthesis:** A typical synthesis procedure is a modification and improvement upon that of previously published work.<sup>[33]</sup> In short,

melamine (12.6 g) was reacted with 37% formaldehyde solution (20 mL) at 85 °C at pH 9.5 (adjusted by 2 M Na<sub>2</sub>CO<sub>3</sub>). Once the solution turned from white (MF dispersion) to clear (MF prepolymer solution), the solution was stirred at 1200 RPM for 15 additional minutes. To follow, the solution was cooled to 40 °C in ambient condition (≈15 min). A 5 wt% Ludox AS 40 aqueous solution (120 g) was added into the solution and continued to be stirred at the same RPM for 20 min. 2 M HCl was then added into the solution until the desired pH was reached and continued to be stirred for 15 min. Afterward, agitation was halted and the solution was allowed to polymerize under stagnant conditions at 40 °C for 4 h. The spherical hollow morphology was strongly dependent on the RPM and polymerization pH. To obtain the hollow morphology the RPM used throughout the synthesis was 1200 RPM and the polymerization pH of 5.5 was used. The reaction was conducted with a cylindrical ≈2 inch Teflon coated metallic stir bar in a 500 mL beaker covered by a watch glass. Afterward the polymer/silica composite was decanted and dried in an oven at 60 °C for 24 h followed by a 180 °C heat treatment for 24 h. The obtained white powder was then carbonized at 900 °C for 2 h with a 5 °C/min ramp rate under argon gas. From thermogravimetric analysis (TGA) analysis of the composite (Figure S9, Supporting Information), the composite was composed of 12% carbon and 88% silica. The resulting powder was washed with an 8 M NaOH solution at 80 °C for 2 days and rinsed with water. After filtering and drying, PEHPC was obtained. pH was measured with a Mettler Toledo S20 SevenEasy pH meter. The sample without silica was synthesized under the same exact conditions except the amount of 2 M HCl was modified to compensate for the lack of basic Ludox additive, still reaching an endpoint of pH 5.5.

PEHPC and sulfur composite was synthesized by mortaring together PEHPC and sulfur at a mass ratio of 30:70 respectively. The mixture was then transferred into a sealed, argon filled Teflon lined autoclave and heated to 155 °C for 12 h. The same procedure was done to synthesize

the Ketjen black 600 JD and sulfur composite. All chemicals were purchased from Sigma-Aldrich.

The blue balloon inflation experiment was performed by first adding 2 M Na<sub>2</sub>CO<sub>3</sub> (0.5 mL) into a 150 mL glass bottle filled with water (100 mL) to increase the pH to 9.5. To follow, 2 M HCl was added into the basic solution until the pH dropped to 5.5 (measured with a Mettler Toledo S20 SevenEasy pH meter). For the experiment with silica, the concentration of silica was kept at 3% (i.e., 7.5 g of 40% wt silica suspension), matching that of material synthesis conditions. It is important to note that the silica suspension is alkaline, therefore the amount of 2 M HCl added was adjusted accordingly to ensure the same amount of CO<sub>2</sub> generation.

**Physical Characterization:** TGA (TA instrument Q500) was conducted under nitrogen atmosphere to confirm the accurate sulfur loading. The protocol entailed a heating rate of 5 °C min<sup>-1</sup> from 25 to 600 °C and maintained at 600 °C for 2 h. Nitrogen sorption (ASAP 2020 micromeritics) was used to retrieve data which was analyzed using Brunauer–Emmett–Teller theory to calculate and in return, characterize the pore size distribution, surface area and pore volume of PEHPC. A Zeiss Leo field-emission scanning electron microscope 1530 was used to characterize the morphology of the material. A JEOL 2010F transmission electron microscope was used to further characterize the morphology of PEHPC. X-ray diffraction (MiniFlex 600 Rigaku) experiments were performed to confirm the removal of silica. XPS was performed using a K-Alpha XPS spectrometer.

**Electrochemical Characterization:** A water based slurry of 15% solid content was formed with the mass ratios of PEHPC/S: carbon nanotubes: sodium carboxymethyl cellulose were 85:5:10, respectively. The slurry was casted onto a carbon coated aluminum foil current collector (MTI Corporation) with a typical sulfur loading of 1.3 ± 0.2 mg<sub>sulfur</sub> cm<sup>-2</sup>. All electrodes were dried at 70 °C for 4 h and transferred into an argon filled glovebox (Labstar MB10 compact, mBraun) with water and oxygen levels both under 1 part per million. The electrochemical performances were evaluated using a 2016 type coin cell with a 1,3-dioxolane and dimethoxyethane electrolyte at a 1:1 ratio with 1 M LiTFSI with 0.2 M lithium nitrate (preblended by BASF). Electrochemical testing station from Neware was used to perform all cycling tests. The electrolyte to sulfur ratio was maintained at 17 μL mg<sup>-1</sup><sub>sulfur</sub> for both cycle life and rate performance tests. The counter and reference electrode used was a lithium metal chip (Linyi Gelon LIB Co., Ltd) while Celgard 2500 was used as the separator. The coin cells were cycled from 2.8 to 1.6 V versus Li/Li<sup>+</sup> for rate performance test and 2.8–1.9 V versus Li/Li<sup>+</sup> to avoid decomposition of LiNO<sub>3</sub>. Electrochemical impedance spectroscopy was performed on a Princeton VersaStat MC with frequency ranges from 100 000 to 0.1 Hz with an amplitude of 50 mV using the same 2016 type coin cells. The EIS circuit was fitted using Zfit software developed by Jean-Luc Dellis, implemented in Matlab. EIS cells were discharged at a constant current of 0.1C with EIS captures taken at once every 1200 s. Shuttle current measurement was performed in accordance to work done by Moy et al.<sup>[31]</sup> Briefly, the cells were first cycled three times (2.8–1.6 V vs Li/Li<sup>+</sup>) at C/20 and then charged to 2.8 V. After leaving at open circuit voltage for 10 min, the cells were held at 2.3 V and the corresponding current was monitored. This experiment was performed using a Princeton VersaStat MC.

## Supporting Information

Supporting Information is available from the Wiley Online Library or from the author.

## Acknowledgements

M.L. and Y.Z. contributed equally to this work. This work was financially supported by the Natural Sciences and Engineering Research Council of Canada (NSERC), University of Waterloo, and the Waterloo Institute for

Nanotechnology. Special thanks to Dr. Carmen Andrei at the Canadian Center for Electron Microscopy at McMaster University for scanning transmission electron microscope, TEM, and EELS analysis. The authors would like to thank Jenny X. Li and Calvin Xu for proof reading.

Received: June 28, 2016

Revised: July 29, 2016

Published online: September 14, 2016

- [1] a) X. Lai, J. E. Halpert, D. Wang, *Energy Environ. Sci.* **2012**, *5*, 5604; b) S. Q. Wang, J. Y. Zhang, C. H. Chen, *Scr. Mater.* **2007**, *57*, 337; c) Z. Y. Wang, L. Zhou, X. W. Lou, *Adv. Mater.* **2012**, *24*, 1903.
- [2] a) H. C. Y. Chen, D. Zeng, Y. Tian, F. Chen, J. Feng, J. Shi, *ACS Nano* **2010**, *4*, 6001; b) J.-F. Chen, H.-M. Ding, J.-X. Wang, L. Shao, *Biomaterials* **2004**, *25*, 723.
- [3] a) J. B. Fei, Y. Cui, X. H. Yan, W. Qi, Y. Yang, K. W. Wang, Q. He, J. B. Li, *Adv. Mater.* **2008**, *20*, 452; b) B. Wang, H. Wu, L. Yu, R. Xu, T. T. Lim, X. W. Lou, *Adv. Mater.* **2012**, *24*, 1111.
- [4] a) Y. F. S. Guo, S. Dong, E. Wang, *J. Phys. Chem. C* **2007**, *111*, 17104; b) A. M. Cao, J. S. Hu, H. P. Liang, L. J. Wan, *Angew. Chem. Int. Ed.* **2005**, *44*, 4391.
- [5] a) D. C. Higgins, Z. Chen, *Can. J. Chem. Eng.* **2013**, *91*, 1881; b) K. Feng, W. Ahn, G. Lui, H. W. Park, A. G. Kashkooli, G. Jiang, X. Wang, X. Xiao, Z. Chen, *Nano Energy* **2016**, *19*, 187; c) J. H. H.-G. Jung, J.-B. Park, Y.-K. Sun, B. Scrosati, *Nat. Chem.* **2012**, *4*, 579.
- [6] a) W. Ahn, D. U. Lee, H. S. Song, S. H. Yeon, K. B. Kim, Z. Chen, *RSC Adv.* **2015**, *5*, 29370; b) X. L. Ji, K. T. Lee, L. F. Nazar, *Nat. Mater.* **2009**, *8*, 500.
- [7] X. Liang, C. Hart, Q. Pang, A. Garsuch, T. Weiss, L. F. Nazar, *Nat. Commun.* **2015**, *6*, 5682.
- [8] a) W. Ahn, M. H. Seo, Y. S. Jun, D. U. Lee, F. M. Hassan, X. Wang, A. Yu, Z. Chen, *ACS Appl. Mater. Interfaces* **2016**, *8*, 1984; b) G. Zhou, E. Paek, G. S. Hwang, A. Manthiram, *Nat. Commun.* **2015**, *6*, 7760.
- [9] N. Jayaprakash, J. Shen, S. S. Moganty, A. Corona, L. A. Archer, *Angew. Chem. Int. Ed.* **2011**, *50*, 5904.
- [10] a) J. Song, M. L. Gordin, T. Xu, S. Chen, Z. Yu, H. Sohn, J. Lu, Y. Ren, Y. Duan, D. Wang, *Angew. Chem. Int. Ed.* **2015**, *54*, 4325; b) J. Song, T. Xu, M. L. Gordin, P. Zhu, D. Lv, Y.-B. Jiang, Y. Chen, Y. Duan, D. Wang, *Adv. Funct. Mater.* **2014**, *24*, 1243; c) Q. Pang, L. F. Nazar, *ACS Nano* **2016**, *10*, 4111.
- [11] a) S.-H. L. D.-R. Chang, S.-W. Kim, H.-T. Kim, *J. Power Sources* **2002**, *112*, 452; b) J. Zheng, D. Lv, M. Gu, C. Wang, J. G. Zhang, J. Liu, J. Xiao, *J. Electrochem. Soc.* **2013**, *160*, A2288; c) G. Ma, Z. Wen, Q. Wang, C. Shen, P. Peng, J. Jin, X. Wu, *J. Power Sources* **2015**, *273*, 511; d) Q. Wang, J. Zheng, E. Walter, H. Pan, D. Lv, P. Zuo, H. Chen, Z. D. Deng, B. Y. Liaw, X. Yu, X. Yang, J. G. Zhang, J. Liu, J. Xiao, *J. Electrochem. Soc.* **2015**, *162*, A474.
- [12] a) H. W. Chen, C. H. Wang, Y. F. Dai, S. Q. Qiu, J. L. Yang, W. Lu, L. W. Chen, *Nano Lett.* **2015**, *15*, 5443; b) L. Zhu, H.-J. Peng, J. Liang, J.-Q. Huang, C.-M. Chen, X. Guo, W. Zhu, P. Li, Q. Zhang, *Nano Energy* **2015**, *11*, 746; c) F. Jin, S. Xiao, L. Lu, Y. Wang, *Nano Lett.* **2016**, *16*, 440; d) H. Kim, J. Lee, H. Ahn, O. Kim, M. J. Park, *Nat. Commun.* **2015**, *6*, 7278.
- [13] J.-Y. Hwang, H. M. Kim, S.-K. Lee, J.-H. Lee, A. Abouimrane, M. A. Khaleel, I. Belharouak, A. Manthiram, Y.-K. Sun, *Adv. Energy Mater.* **2016**, *6*, 1501480.
- [14] a) C. Zhang, H. B. Wu, C. Yuan, Z. Guo, X. W. Lou, *Angew. Chem. Int. Ed.* **2012**, *124*, 9730; b) X. Wang, G. Li, J. Li, Y. Zhang, A. Wook, A. Yu, Z. Chen, *Energy Environ. Sci.* **2016**, *9*, 2533; c) W. Zhou, X. Xiao, M. Cai, L. Yang, *Nano Lett.* **2014**, *14*, 5250; d) S. Liu, Y. Li, X. Hong, J. Xu, C. Zheng, K. Xie, *Electrochim. Acta* **2016**, *188*, 516.

- [15] A. Manthiram, S. H. Chung, C. Zu, *Adv. Mater.* **2015**, *27*, 1980.
- [16] J. Zheng, M. Gu, M. J. Wagner, K. A. Hays, X. Li, P. Zuo, C. Wang, J. G. Zhang, J. Liu, J. Xiao, *J. Electrochem. Soc.* **2013**, *160*, A1624.
- [17] a) J. Liu, T. Yang, D. W. Wang, G. Q. Lu, D. Zhao, S. Z. Qiao, *Nat. Commun.* **2013**, *4*, 2798; b) J. Tang, J. Liu, R. R. Salunkhe, T. Wangd, Y. Yamauchi, *Chem. Commun.* **2016**, 52, 55.
- [18] a) P. Guo, H. Song, X. Chen, *J. Mater. Chem.* **2010**, *20*, 4867; b) Y. Xia, B. Wang, X. Zhao, G. Wang, H. Wang, *Electrochim. Acta* **2016**, *187*, 55.
- [19] S. U. Pickering, *J. Chem. Soc.* **1907**, 196, 2001.
- [20] a) U. T. Gonzenbach, A. R. Studart, E. Tervoort, L. J. Gauckler, *Angew. Chem., Int. Ed.* **2006**, *45*, 3526; b) H. Hassander, B. Johansson, B. Törnell, *Colloids Surf.* **1989**, *40*, 93; c) E. Vignati, R. Piazza, T. P. Lockhart, *Langmuir* **2003**, *19*, 6650; d) E. Dickinson, *Trends Food Sci. Technol.* **2012**, *24*, 4; e) E. Dickinson, *Curr. Opin. Colloid Interface Sci.* **2010**, *15*, 40; f) B. P. Binks, T. S. Horozov, *Angew. Chem.* **2005**, *117*, 3788; g) R. M. Bernard, P. Binks, S. P. Armes, S. Fujii, A. Schmid, *Langmuir* **2007**, *23*, 8691.
- [21] a) E. N. Brown, M. R. Kessler, N. R. Sottos, S. R. White, *J. Microencapsulation* **2010**, *20*, 719; b) S. Omi, Y. Shiraishi, H. Sato, H. Kubota, *J. Chem. Eng. Jpn.* **1968**, *2*, 64; c) K. L. Thompson, C. J. Mable, J. A. Lane, M. J. Derry, L. A. Fielding, S. P. Armes, *Langmuir* **2015**, *31*, 4137.
- [22] a) F. Sebra, *J. Colloid Interface Sci.* **1970**, *35*, 643; b) X. Gao, L.-J. Wang, C. Wu, Y.-W. Cheng, X. Li, *Ind. Eng. Chem. Res.* **2013**, *52*, 10835; c) P. Taylor, *Adv. Colloid Interface Sci.* **1998**, *75*, 107.
- [23] T. M. H. Daiguji, H. Kinoshita, T. Oyabu, F. Takemura, *J. Phys. Chem. B* **2007**, *111*, 8879.
- [24] a) J. Zhou, X. Qiao, B. P. Binks, K. Sun, M. Bai, Y. Li, Y. Liu, *Langmuir* **2011**, *27*, 3308; b) F. F. Fang, Y. D. Liu, H. J. Choi, *Smart Mater. Struct.* **2010**, *19*, 124002; c) M. Nawaz, W. Miran, J. Jang, D. S. Lee, *Catal. Today* 10.1016/j.cattod.2016.02.017.
- [25] Q. Pang, J. Tang, H. Huang, X. Liang, C. Hart, K. C. Tam, L. F. Nazar, *Adv. Mater.* **2015**, *27*, 6021.
- [26] a) Y. Li, T. T. Li, M. Yao, S. Q. Liu, *J. Mater. Chem.* **2012**, *22*, 10911; b) R. Jia, J. Chen, J. Zhao, J. Zheng, C. Song, L. Li, Z. Zhu, *J. Mater. Chem.* **2010**, *20*, 10829; c) J. Han, G. Xu, B. Ding, J. Pan, H. Dou, D. R. MacFarlane, *J. Mater. Chem. A* **2014**, *2*, 5352; d) S. Feng, W. Li, Q. Shi, Y. Li, J. Chen, Y. Ling, A. M. Asiri, D. Zhao, *Chem. Commun.* **2014**, 50, 329; e) M. Y. Song, D.-S. Yang, K. P. Singh, J. Yuan, J.-S. Yu, *Appl. Catal., B* **2016**, *191*, 202; f) Y. Wen, B. Wang, B. Luo, L. Wang, *Eur. J. Inorg. Chem.* **2016**, 2016, 2051; g) G. M. Zhou, Y. B. Zhao, A. Manthiram, *Adv. Energy Mater.* **2015**, *5*, 1402263; h) F. Pei, T. An, J. Zang, X. Zhao, X. Fang, M. Zheng, Q. Dong, N. Zheng, *Adv. Energy Mater.* **2016**, *6*, 1502539.
- [27] X. G. Sun, X. Wang, R. T. Mayes, S. Dai, *ChemSusChem* **2012**, *5*, 2079.
- [28] D. Lv, J. Zheng, Q. Li, X. Xie, S. Ferrara, Z. Nie, L. B. Mehdi, N. D. Browning, J.-G. Zhang, G. L. Graff, J. Liu, J. Xiao, *Adv. Energy Mater.* **2015**, *5*, 1402290.
- [29] L. Yuan, X. Qiu, L. Chen, W. Zhu, *J. Power Sources* **2009**, 189, 127.
- [30] T. Z. Hou, X. Chen, H. J. Peng, J. Q. Huang, B. Q. Li, Q. Zhang, B. Li, *Small* **2016**, *12*, 3283.
- [31] D. Moy, A. Manivannan, S. R. Narayanan, *J. Electrochem. Soc.* **2014**, *162*, A1.
- [32] a) J. L. L. Wang, S. Yuan, Y. Wang, Y. Xia, *Energy Environ. Sci.* **2016**, *9*, 224; b) L. Wang, Y. G. Wang, Y. Y. Xia, *Energy Environ. Sci.* **2015**, *8*, 1551; c) S. Chen, F. Dai, M. L. Gordin, Z. Yu, Y. Gao, J. Song, D. Wang, *Angew. Chem. Int. Ed.* **2016**, *55*, 4231.
- [33] H. Nie, H. Zhang, Y. Zhang, T. Liu, J. Li, Q. Lai, *Nanoscale* **2013**, *5*, 8484.